



# Estimation of losses caused by sidewall roughness in thin-film lithium niobate rib and strip waveguides

MANFRED HAMMER,<sup>1,2,3,\*</sup>  SILIA BABEL,<sup>3,4</sup>   
HENNA FARHEEN,<sup>1,3</sup>  LAURA PADBERG,<sup>3,4</sup>  
J. CHRISTOPH SCHEYTT,<sup>2,3</sup>  CHRISTINE SILBERHORN,<sup>3,4</sup>   
AND JENS FÖRSTNER<sup>1,3</sup> 

<sup>1</sup>Theoretical Electrical Engineering, Paderborn University, Paderborn, Germany

<sup>2</sup>System and Circuit Technology, Heinz Nixdorf Institute, Paderborn University, Paderborn, Germany

<sup>3</sup>Institute for Photonic Quantum Systems (PhoQS), Paderborn University, Paderborn, Germany

<sup>4</sup>Integrated Quantum Optics, Paderborn University, Paderborn, Germany

\*[manfred.hammer@uni-paderborn.de](mailto:manfred.hammer@uni-paderborn.de)

**Abstract:** Samples of dielectric optical waveguides of rib or strip type in thin-film lithium niobate (TFLN) technology are characterized with respect to their optical loss using the Fabry-Pérot method. Attributing the losses mainly to sidewall roughness, we employ a simple perturbational procedure, based on rigorously computed mode profiles of idealized channels, to estimate the attenuation for waveguides with different cross sections. A single fit parameter suffices for an adequate modelling of the effect of the waveguide geometry on the loss levels.

© 2024 Optica Publishing Group under the terms of the [Optica Open Access Publishing Agreement](#)

## 1. Introduction

Integrated photonics fosters the development of high-performance devices that are scalable, energy-efficient, and have a small-footprint by integrating various passive and active optical components onto a single platform. This can improve the performance and stability of optical systems for data communication, sensing, imaging, and quantum information processing. Driven by these applications, thin-film lithium niobate (TFLN) / lithium niobate on insulator (LNOI) has emerged as a strong material platform because of its high non-linearity and electro-optic properties [1]. The high modal confinement of thin-film lithium niobate waveguides allows for compact devices with small bend radii [2]. Moreover, LNOI is a suitable candidate for efficient non-linear devices [2–6] and fast electro-optic modulators [7–12].

Low-loss waveguide channels can be expected to be highly relevant for future high-performance photonic devices. Concerning the LNOI platform, the unstructured thin-film material has intrinsic losses (0.2 dB/m [13]) that are somewhat higher than the levels for bulk lithium niobate, probably as a consequence of the ion implantation damage incurred during fabrication [13]. Structured channels made from these thin-film slabs exhibit even higher attenuation, mostly caused by rough sidewalls. To mitigate this effect, the device can be clad with materials such as SiO<sub>2</sub> to reduce the refractive index contrast, the roughness can be lowered by tuning the fabrication process, or the overlap of the optical mode with the sidewalls can be reduced by accepting multi-mode waveguide geometries [14]. Using these approaches a lowest propagation loss of 1 dB/m around 1550 nm has been demonstrated in 2023 [15]. Low losses are deemed to be essential in particular in contexts of quantum optics [16], single photon processing [17], or optical quantum computing [18]. Understanding the limitations of these systems is essential and therefore also techniques to model and estimate optical losses are important in these fields.

Among the various sources of loss that impact the functioning of integrated photonic circuits, the roughness of dielectric interfaces, and the irregular, extrinsic scattering of optical power

effected by it [19], is perhaps the most elusive, the least amenable to direct theoretical modelling. While early approaches [20,21] derive approximate analytical expressions for the scattering loss caused by irregularities at the core interfaces of slab waveguides (1-D cross sections, TE polarization/waves), later also channel waveguides with 2-D cross sections were considered [22]. Here the studies include rectangular strips with corrugated (strictly vertical) sidewalls, with results for waveguides in Si/SiO<sub>2</sub>-technology [23] and for TE- and TM-like modes of Si<sub>3</sub>N<sub>4</sub>/SiO<sub>2</sub> waveguides [24]. Beyond a largely analytical, approximate treatment [22] based on results [20] for slab waveguides, the actual scattering has been modelled by volume current methods [24–27] on the basis of numerically computed modes of the idealized channels, also for strip waveguides with a lateral photonic crystal “cladding” [25], and for rib waveguides with inhomogeneous external layering, then on the basis of rigorous finite element solutions for the external scattered fields [26]. Further, coupled-mode techniques are employed, for rectangular channels in a homogeneous background and coupling to forward and backward traveling guided and radiation modes [28,29]. While the models mentioned before consider a roughness in “one dimension” only, such as the randomly longitudinally varying lateral position of an otherwise strictly vertical channel sidewall (random grooves), a more recent study derives loss estimates for “two-dimensional” roughness (random dust), restricted to rectangular strip waveguides in a homogeneous exterior [27].

Typically, these approaches require a statistical description of the sidewall roughness, obtained e.g. by atomic force microscopy (AFM) [28] or scanning electron microscopy (SEM) [30], in the form of an exponential or Gaussian autocorrelation function, with the correlation length and the mean square deviation from a flat surface as characterizing parameters. For specific geometries of waveguide core and exterior, and given the mostly numerically computed modes of the ideal, smooth channels, the models then predict modal attenuation constants and loss levels.

A common finding is that the loss coefficients are proportional to the square of the difference between the permittivity levels of the media at both sides of the rough interfaces. Selection of these media is closely related to the choice of a particular technological platform. Also, the attenuation is proportional to the strength of the roughness, the mean square deviation from the flat surface. Assuming that one aims at low losses, fabrication procedures need to be tuned to produce surfaces as smooth as possible. Further, the models roughly agree that the attenuation constant of any specific mode is proportional to the square of the relative electric field strengths of its normalized profile at the interfaces in question. This last observation forms the basis for the procedure that we discuss in this paper.

Initially, we are faced with the following task: Given a few measurements for typical, practically relevant TFLN waveguides, modal loss levels for comparable waveguides with different cross section geometry are to be estimated. With slanted sidewalls, anisotropic core, and inhomogeneous layered exterior, our samples do not fit any of the sophisticated models mentioned before. Adaptation might be possible, but will probably be expensive in terms of both analytical and computational overhead. Further, beyond images of waveguide cross sections, no experimental characterization of the actual statistical sidewall corrugation of our samples is directly available.

Hence, as a more pragmatic approach, we loosely follow the arguments of Ref. [31]. The surface roughness is represented by thin lossy layers at the waveguide sidewalls. Imaginary parts of refractive indices, or permittivity, respectively, are introduced as fit parameters. In place of iterated modal analysis of the resulting waveguides with local complex permittivity, we apply perturbation theory [32] to simplify the fit procedure, and to predict modal attenuation coefficients. The perturbational expressions are in line with the notion that the losses are driven by the squared local modal electric field strength.

Our respective procedure for the estimation of losses due to sidewall surface roughness, and its results, are discussed in Sections 5 and 6. In previous Sections 2 – 4, we introduce our sample

parameters, add a few more general remarks on the optical losses, and report on the fabrication and characterization.

## 2. Waveguide samples

Trapezoidal TFLN waveguides of rib or strip type are considered, with cross sections as introduced in Fig. 1, for guided wave propagation at vacuum wavelength  $\lambda = 1.55 \mu\text{m}$ . Isotropic silicon-oxide substrate/buffer and cladding layers with refractive indices  $n_s = n_c = 1.45$ , and an air cover ( $n_a = 1.0$ ) enclose the anisotropic lithium niobate (LN) core layer with permittivity  $\hat{\epsilon}_f$ .

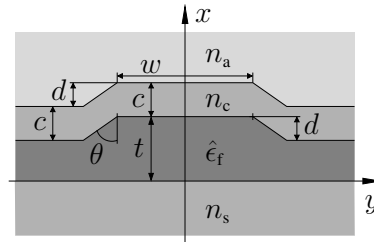


**Fig. 1.** Potentially lossy LNOI waveguide, cross section. Cartesian coordinates  $x, y$  span the cross section plane, with the  $x$ -axis oriented perpendicular to the substrate. The  $z$ -axis (not shown) indicates the propagation direction. Media, parameters: substrate refractive index  $n_s$ , core permittivity  $\hat{\epsilon}_f$ , cladding refractive index  $n_c$ , cover refractive index  $n_a$ . Dimensions: waveguide top-width  $w$ , core film thickness  $t$ , etching depth  $d$ , cladding thickness  $c$ , sidewall angle  $\theta$ .

The LNOI waveguides are prepared in the “X-cut, Y-propagation”-configuration. Referring to the coordinates of Fig. 1, the core medium is characterized by a relative permittivity  $\hat{\epsilon}_f$  of the form [33]





$$\hat{\epsilon}_f = \begin{pmatrix} n_o^2 & 0 & 0 \\ 0 & n_e^2 & 0 \\ 0 & 0 & n_o^2 \end{pmatrix}, \quad (1)$$

with ordinary and extraordinary refractive indices  $n_o = 2.1836$  and  $n_e = 2.1220$ . Here we adopt data from measurements of LN thin-film properties [33,34], for the target wavelength  $\lambda = 1.55 \mu\text{m}$ .

Four waveguide samples are available, two of which are rib waveguides with a partly etched core layer, the other two are fully etched strip waveguides, in both cases with channels of different widths. The layer stacks differ in core and cladding thickness. Table 1(a) collects the respective geometrical parameters.

The samples are supported by a further lithium niobate layer, the actual substrate (“handle”), beneath the  $2 \mu\text{m}$  thick lower oxide buffer. A simple complex slab waveguide solver [35] can be used for a rough estimate of any leakage incurred: With the material parameters ( $n_e$  and  $n_o$  averaged) and thicknesses of the central layer stacks of our samples, and a substrate refractive index of  $\approx 2.2$  (bulk LN), one obtains attenuation constants that are orders of magnitude below the levels observed for the channels (Table 1(b)). We conclude that the oxide buffer isolates the guiding region sufficiently from the substrate. For the further discussion, the oxide can thus be regarded half-infinite, as indicated in Fig. 1.

**Table 1. (a) Waveguide samples, parameters according to Fig. 1: film thickness  $t$ , etching depth  $d$ , top width of the rib  $w$ , cladding thickness  $c$ , and sidewall angle  $\theta$ . (b) Loss measurements and loss estimates, data per sample ID and measured polarization. Rows: polarization ratio  $\Pi$  (Eq. (9)), modal effective index  $N_{\text{eff}}$ , estimated loss parameter  $\epsilon''$ , and measured and estimated losses  $L$  and attenuation coefficients  $\alpha$ . Procedure identifiers: (M): measurements, (S): simulations, (E): estimates, for a roughness layer of thickness  $s = 20$  nm,  $\epsilon'' = 0.0194$ .**

(a) LNOI . . .		600b13	600b29	450b14(1)		450b14(2)	
$t$ [nm]		600	600	450		450	
$d$ [nm]		150	150	450		450	
$w$ [ $\mu\text{m}$ ]		1.0	1.3	1.7		1.1	
$c$ [nm]		150	150	600		600	
$\theta$ [ $^\circ$ ]		60	60	56		56	
							
(b) LNOI . . .		600b13	600b29	450b14(1)	450b14(1)	450b14(2)	450b14(2)
	(M)	TE	TE	TE	TM	TE	TM
$\Pi$	(S)	1.00	1.00	1.00	0.39	1.00	0.04
$N_{\text{eff}}$	(S)	1.91967	1.92647	1.85828	1.78819	1.83836	1.76598
$\epsilon''$ [ $10^{-2}$ ]	(M,S)	$1.8 \pm 0.4$	$2.0 \pm 0.2$	$2.3 \pm 0.3$	$2.1 \pm 0.3$	$1.7 \pm 0.2$	$2.3 \pm 0.3$
$\alpha/k$ [ $10^{-5}$ ]	(M)	$1.38 \pm 0.27$	$1.09 \pm 0.11$	$1.46 \pm 0.18$	$2.58 \pm 0.39$	$2.43 \pm 0.22$	$2.66 \pm 0.31$
	(E)	1.48	1.08	1.22	2.34	2.81	2.24
$L$ [dB/cm]	(M)	$4.85 \pm 0.95$	$3.83 \pm 0.38$	$5.13 \pm 0.65$	$9.07 \pm 1.39$	$8.57 \pm 0.79$	$9.36 \pm 1.08$
	(E)	5.21	3.79	4.29	8.25	9.89	7.87

### 3. Propagation losses

For the theoretical considerations in this paper, we adopt a frequency domain description. All electromagnetic fields are assumed to vary periodically in time  $\sim \exp i\omega t$  with angular frequency  $\omega = kc = 2\pi c/\lambda$ , for vacuum wavenumber  $k$ , wavelength  $\lambda$ , and vacuum speed of light  $c$ .

This concerns potentially lossy guided modes supported by the channels, with a dependence of the optical fields on the propagation distance  $z$  of the form  $\sim \exp(-i(\beta - i\alpha)z)$ , with real phase propagation constant  $\beta$  and real attenuation constant  $\alpha$ . For the propagation of a single guided mode, the local optical power carried by that mode varies as  $\sim \exp(-2\alpha z)$ . Over a distance  $z$ , the power loss  $l$  in decibel units is  $l = -10 \log_{10}(\exp(-2\alpha z))$ , such that the attenuation constant can be expressed in terms of the loss per distance as  $\alpha = 0.05 \ln(10) l/z$ . Measured loss values  $L$  are available in units of dB/cm, which thus translate to attenuation constants as

$$\alpha = 0.05 \ln(10) L. \quad (2)$$

It might be tempting to compare the modal losses with the values observed for plane wave propagation through a potentially lossy (isotropic) bulk medium with complex refractive index  $n = n' - in''$ , for real  $n'$ ,  $n''$ . In that case the optical fields depend on propagation distance  $z$  as  $\sim \exp(-ikn'z) \exp(-kn''z)$ ; the losses in power  $L$  per distance translate to imaginary parts of refractive indices as  $n'' = \ln(10)/(40\pi) \lambda L \approx 0.01832 \lambda L$ . In this context we like to emphasize that the losses associated with some bulk medium *do not establish a lower limit* for modal losses of waveguides with a core made from this medium. Even for an idealized, perfectly smooth waveguide, modal losses can well be lower or (slightly) higher than the bulk losses associated with the waveguide core medium [36,37]. Roughly, this can be realized as follows: On the one hand, the guided wave travels only partly through the lossy core, and partly through the adjoining media with potentially lower attenuation (see e.g. the mode profiles in Fig. 4). On the other hand,

the light path associated with the guided wave propagation in the core is longer than the path for a plane wave propagating straight along the waveguide axis.

Anyway, the LiNbO<sub>3</sub> core medium of the present waveguides can be associated with low bulk losses of about 0.2 dB/m only, related to a plane wave attenuation constant  $kn''$  with  $n'' = 6 \cdot 10^{-9}$  [13,38]. Likewise, the measurements on non-structured LNOI samples in [33,34] do not indicate any loss levels that would be significant when compared to the values in Table 1(b). We can therefore reasonably assume that the losses as observed for our samples are introduced in the subsequent channel structuring process. In Section 5, we attribute the attenuation exclusively to roughness-induced scattering at the slanted sidewalls of the LN strip (cf. Figure 5), as the dominant effect. Clearly, this must be regarded as a simplifying assumption. Other, probably smaller, contributions, not covered by our model, can be expected from the bulk attenuation of the cladding medium, from irregularities at the horizontal “top” LN/SiO<sub>2</sub> and SiO<sub>2</sub>/air interfaces, and from the slanted outer SiO<sub>2</sub>/air interfaces. The latter are formed by chemical deposition, and are therefore smooth when compared to the LN/SiO<sub>2</sub> boundary, which is defined by particle bombardment. Further, the relative modal field strength is much lower at the outer than at the inner slanted interfaces (see the profiles in Figs. 4 and 7).

Lateral leakage [39] should perhaps be mentioned here as another potential source of propagation loss, for straight waveguides of rib type similar to samples LNOI600b13 and LNOI600b29. This can occur for “nearly-guided” modes in regimes of shallow etching or narrow channels, and is typically encountered for TM polarization. Note that a rigorous theoretical assessment based on the properties of slab modes guided by the external lateral layer stacks should certainly include the core anisotropy. Our numerical analysis of the (idealized) samples, however, predicts that both support strictly guided modes with TE- as well as TM-like polarization (cf. Fig. 6(a)).

#### 4. Sample preparation and loss measurements

The waveguides are fabricated by a physical dry etching process with an etching mask consisting of SiO<sub>2</sub> produced via a lift-off process [40]. Therefore, on the cleaned sample we apply a photo resist and structure it by using a laser lithography system (Heidelberg Instruments DWL 66+). As a next step, we develop the sample and deposit SiO<sub>2</sub> on top of it via a sputtering process (Prevac Sputtering system 518). After the lift off process, we etch the structure given by the SiO<sub>2</sub> etching mask in the LN thin-film via a dry etching process with a pure Argon plasma (Oxford Instruments Plasmalab System 100). We apply a SiO<sub>2</sub> cladding layer on top and prepare the end-facet of each sample by chemo-mechanical polishing (cf. Ref. [41] for a similar procedure). All investigated samples are produced with roughly the same process such that it can be assumed that the loss-generating surface roughness is comparable.

To characterize the samples we apply the Fabry-Pérot method [42]. The waveguide segments are regarded as Fabry-Pérot resonators in which the polished end-facets act as mirrors. The setup for this measurement is depicted in Fig. 2. It consists of a tunable CW-laser at 1550 nm (Santec TSL-550) which is fiber-coupled. A fiber polarization controller is used to set the polarization. With a lens the light is coupled to free-space and two mirrors guide the light towards the sample. Aspheric lenses then couple the light into and out of the sample. Afterwards the transmission is measured with a power sensor (Thorlabs Powermeter PM400 and S122C/S132C).

All measured waveguides have a length between 7 and 8 mm. Their end-facet reflectivity is calculated [43] using the FDTD solver of Lumerical. To determine the losses, a wavelength scan from 1550 nm to 1550.5 nm in 3 pm steps is performed, and the transmitted intensity is measured, without a discrimination of polarization. The change in the wavelength effects a change of the resonance condition of the Fabry-Pérot resonator. This leads to constructive and destructive interference of the light, and oscillations in the transmitted power can be observed (see Fig. 3).

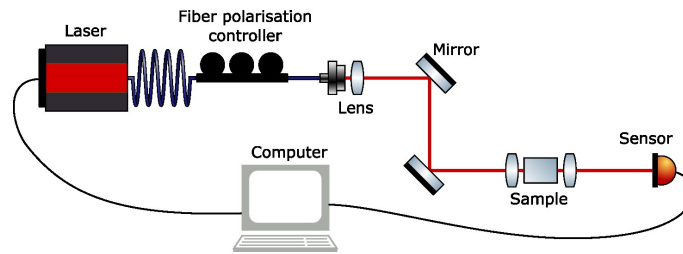


**Fig. 2.** Setup for the Fabry-Pérot loss measurement.

Losses are then calculated from the contrast of these oscillations, the end-facet reflectivity, and the length of the samples.

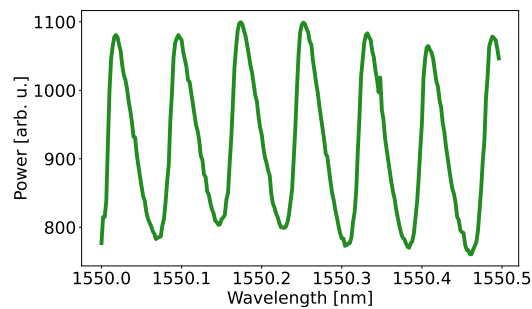


**Fig. 3.** Measured intensity as a function of the wavelength from an LNOI waveguide sample. The wavelength change leads to oscillations by varying the resonance conditions. From these the losses can be estimated by calculating the contrast.

This procedure leads to the values for losses (row  $L$  (M)) and attenuation constants (row  $\alpha/k$  (M)) as listed in Table 1(b). Results for TM polarization are not available for samples LNOI600b13 and LNOI600b29. According to Fig. 6(a), both channels should support guided TM-like modes. These, however, are “only just guided” fields close to cutoff, with rather wide, laterally weakly confined profiles, where almost all parameters that enter the simulations could easily affect the guidance prediction. Respective loss measurements for TM polarization have not been conclusive.

## 5. Loss modelling

Our estimation procedure is based on the lossless guided modes of the idealized waveguides, with smooth dielectric interfaces. We apply the finite-element solver included in the JCMwave software suite [44] to compute propagation constants  $\beta = kN_{\text{eff}}$ , effective indices  $N_{\text{eff}}$ , and vectorial mode profiles with electric parts  $\mathbf{E}$  and magnetic parts  $\mathbf{H}$ . The solver operates on a computational window  $(x, y) \in [-2, 2] \times [-Y, Y] \mu\text{m}$ , where  $Y = 3 \mu\text{m}$  if  $w \leq 1.7 \mu\text{m}$ , and  $Y = w/2 + 2.15 \mu\text{m}$  otherwise, for waveguides with a top width  $w$ , with boundary conditions of PEC type at the top and bottom boundaries, and transparent conditions at the left and right boundaries of the domain. Adaptive mesh refinement and a symmetry condition at  $y = 0$  are enabled (cf. Fig. 1). For our samples, we obtain the profiles shown in Fig. 4; Table 1(b) lists the associated effective indices.

In line with the recipes from Ref. [31] we assume that the scattering losses originate from thin layers at the waveguide sidewalls. Somewhat arbitrarily, we choose a shape as shown in Fig. 5, with a thickness  $s = 20 \text{ nm}$ , if not specified otherwise. In these regions, indicated by the symbol



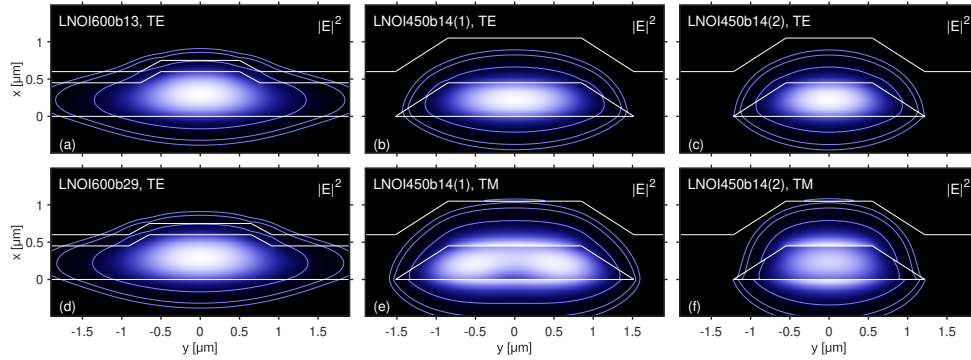


**Fig. 4.** Modes supported by the four sample waveguides, lowest order profiles with dominant polarization as indicated; the absolute square  $|E|^2$  of the optical electric field associated with the modes is shown.

□ in the following arguments, the local permittivity  $\hat{\epsilon}_f$  is modified by some “small” contribution  $\delta\hat{\epsilon}$  that represents the roughness.  $\delta\hat{\epsilon}$ , or variables that define this quantity, will be considered as fit parameters.

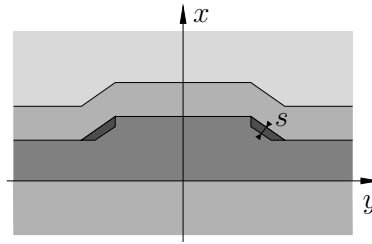


**Fig. 5.** Modelling of surface roughness: Layers of thickness  $s$  at the rib sidewalls (“inside” the rib, shaped as illustrated) are assumed to consist of a material with complex permittivity that differs from the core value.

Other choices for the region □ are possible and can be made plausible, such as a parallelogram that includes part of the top interface of the LN rib, or a region that extends further downwards into the lateral LN slab, to model potential detritus-filled grooves left by the etching process next to the rib. In any case, the perturbation is meant to probe the modal field “at the rib sidewalls”; modestly different definitions of that region can be expected to have only very minor influence on the predictions of attenuation and loss, just as shown later for the thickness parameter  $s$ .

Next, standard perturbational expressions [32] are applied to predict the effect of the lossy region. Assuming that the profile  $\mathbf{E}$ ,  $\mathbf{H}$  of a particular mode with propagation constant  $\beta$  supported by a waveguide with permittivity  $\hat{\epsilon}$  is an adequate approximation of the modal solution for the waveguide with permittivity  $\hat{\epsilon} + \delta\hat{\epsilon}$ , the respective mode propagates through the perturbed waveguide with a propagation constant  $\beta + \delta\beta$ , where, in first order, the difference  $\delta\beta$  is given through the integral

$$\delta\beta = \frac{\omega\epsilon_0}{4P} \iint \mathbf{E}^* \cdot \delta\hat{\epsilon} \mathbf{E} \, dx \, dy \quad \text{with} \quad P = \frac{1}{2} \text{Re} \iint (E_x^* H_y - E_y^* H_x) \, dx \, dy. \quad (3)$$

Here the modal power  $P$  normalizes the profile.

The waveguides are potentially attenuating. We therefore choose a perturbation

$$\delta\hat{\epsilon}(x, y) = \begin{cases} -i\epsilon''1, & \text{for } (x, y) \in \square, \\ 0 & \text{elsewhere,} \end{cases} \quad (4)$$

parameterized by the local imaginary part  $\epsilon''$  of the permittivity, with unit matrix 1. Then, according to Eq. (3), the propagation constant of the mode in the lossy waveguide is  $\beta - i\alpha$ , with an attenuation constant

$$\alpha = Q\epsilon'' \quad \text{with} \quad Q = \frac{\omega\epsilon_0}{4P} \iint_{\square} |E|^2 dx dy. \quad (5)$$

The integral ratio (“overlap”)  $Q$  represents the relative squared field strength of the mode profiles at the sidewalls. Obviously,  $Q$  changes with the mode and waveguide under consideration. On the basis of numerically computed mode profiles, discretized on a suitably dense mesh, the values  $Q$  are evaluated by Gaussian quadrature [45]; modal symmetry can be exploited.

Now we consider briefly the loss parameters associated with the individual measurements. Having computed the overlaps  $Q_m$  on the basis of the profiles of Fig. 4, values  $\epsilon_m''$  are estimated as ratios  $\epsilon_m'' = \alpha_m/Q_m$ , where the loss levels for measurements  $m$  are translated to attenuation coefficients  $\alpha_m$  by Eq. (2). Despite the differences between the samples, Table 1 (row  $\epsilon''$  (M,S)) shows an excellent agreement of the values  $\epsilon_m''$  determined for the separate measurements. Apparently, the simple perturbational model captures adequately the influence of the waveguide geometry, and of the modal field shape, including polarization, on the sidewall scattering losses.

Obviously, the values obtained for the loss parameters  $\epsilon_m''$  obtained in this way depend on the chosen thickness  $s$  of the imagined roughness layer. As long as  $s$  is sufficiently small (the layer is meant to probe electric fields “at the interface”), such that the field variation over  $s$  can be neglected for the integral, both  $Q$  and the estimate  $1/\epsilon_m''$  are roughly proportional to  $s$ . The dependence cancels in Eq. (5). We checked this explicitly for the six measurements; for  $s \in \{10, 40\}$  nm,  $(\alpha_m/Q_m)s/(20 \text{ nm})$  deviates by no more than 0.0016 from the values for  $s = 20$  nm in the table. Any attenuation coefficients estimated with these values should thus be reasonably independent from the particular values of  $s$ .

In order to characterize the roughness properties of the waveguide sidewalls, a single best value  $\epsilon''$  for our fit parameter is required. The measured loss levels and the related attenuation coefficients  $\alpha_m$  come with error margins  $\Delta\alpha_m$ . We thus apply a procedure for “weighted least squares” or “ $\chi$ -square” fitting [45]. Minimizing the weighted error  $D(\epsilon'') = \sum_m (\alpha_m - Q_m\epsilon'')^2 / \Delta\alpha_m^2$  leads to the recipe

$$\epsilon'' = \left( \sum_m \frac{1}{\Delta\alpha_m^2} \alpha_m Q_m \right) / \left( \sum_m \frac{1}{\Delta\alpha_m^2} Q_m^2 \right) \quad (6)$$

for determining  $\epsilon''$ . Here the sums run over all measurements  $m$ . Equation (6) can be viewed as a weighted mean of the individual loss parameters  $\epsilon_m''$ ,

$$\epsilon'' = \left( \sum_m w_m \epsilon_m'' \right) / \left( \sum_m w_m \right), \quad (7)$$

with weights  $w_m = Q_m^2 / \Delta\alpha_m^2$ , a related weighted standard deviation  $\Delta\epsilon''$ , and weighted variance

$$(\Delta\epsilon'')^2 = \left( \sum_m w_m (\epsilon_m'' - \epsilon'')^2 \right) / \left( \frac{M-1}{M} \sum_m w_m \right). \quad (8)$$

Here  $M$  is the number of data points. The mode profile overlaps  $Q_m$  (Eq. (5)), for a roughness layer thickness  $s = 20$  nm, and the measured attenuation constants  $\alpha_m$  and error margins  $\Delta\alpha_m$  from Table 1 (row  $\alpha/k$  (M)), lead to values  $\epsilon'' = 0.0194$  and  $\Delta\epsilon'' = 0.0027$  for our loss parameter.



For a benchmark, we then re-estimate the losses and attenuation coefficients for all measurements, using the perturbational integrals (5) with this optimum  $\epsilon''$ . The respective results in Table 1 (labels (E)) show a satisfying agreement with the actual measurement data (labels (M)).

## 6. Loss estimates

Given the former measurements and estimation procedure, loss levels can be predicted for waveguides with different but reasonably similar geometries. Assuming a left-right mirror symmetric structure and fixed media properties, Fig. 1 introduces in total five geometrical parameters, all of which must be expected to affect the scattering losses in the one or other way, in principle. Among these, the “thickness-related” parameters (here  $c$ ,  $t$ ,  $d$ , and partly also  $\theta$ ) are linked to the processes of layer deposition (LN cutting) and etching, and are therefore typically chosen once for an entire chip or wafer, with values potentially limited by a foundry or multi-project-wafer run, if applicable. Contrarily, the waveguide top width  $w$  can be easily and rather arbitrarily adjusted through the definition of the etching masks. Hence we focus on variations of  $w$  as the most tangible parameter, with the other quantities as given by our samples. Obviously, it is assumed that the same fabrication processes are applied, such that one can expect comparable surface roughness. Figures 6(b) and 6(d) show respective estimates for waveguide configurations of varying widths. For each  $w$ , numerical mode analysis yields effective indices  $N_{\text{eff}}$  and mode profiles for potentially several guided modes. For each of these, the profiles then serve to compute overlaps  $Q$ , and, through Eq. (5), separate attenuation coefficients and loss levels.

The effective indices are limited, at large widths  $w$ , by the levels of effective indices of the fundamental 1-D modes supported by multilayer slab waveguides with the layer stack of the core region of the present channels. According to Eq. (1), in the LN layer the ordinary refractive index  $n_o$  is relevant for TM slab modes with predominantly  $x$ -oriented electric fields. Likewise,  $y$ -polarized TE slab modes are governed by the extraordinary refractive index  $n_e$ . Figures 6(a) and 6(c) show respective upper limiting levels for the effective indices [46]. Lower limits are given, for the ribs in Fig. 6(a, b), by the fundamental slab mode of the outer, thinner layer stack, or, for the strip waveguides in Fig. 6(c, d), by the refractive index of the substrate (buffer) layer.

The figures include additional attributes of the modal solutions. The waveguides in question are mirror symmetric with respect to the central  $x$ - $z$ -plane at  $y = 0$  (cf. Fig. 1). All modes supported by these are of a specific parity; their electromagnetic field components show a specific symmetry. Table 2 summarizes these properties, and associates the parity class with standard mode identifiers, for the present case of “vertically single mode”, slab-like waveguides. Modes that differ in parity can be degenerate; the respective curves  $N_{\text{eff}}$  vs.  $w$  in Figs. 6(a) and 6(c) can cross. Modes that share the same parity class cannot be degenerate; the associated curves “repel” each other. The panels of Fig. 6 show the modal parity through different marker symbols.

**Table 2. Classes of modal parity, symmetry of field profile components (even: +, odd: -), and associated mode identifiers**

	$E_x$	$E_y$	$E_z$	$H_x$	$H_y$	$H_z$	
SYM	-	+	-	+	-	+	TE <sub>00</sub> , TM <sub>01</sub> , TE <sub>02</sub> , TM <sub>03</sub> , ...
ASY	+	-	+	-	+	-	TM <sub>00</sub> , TE <sub>01</sub> , TM <sub>02</sub> , TE <sub>03</sub> , ...

Further, the present waveguides support hybrid modes that are more or less well polarized in either TE- ( $y$ ) or TM-direction ( $x$ ,  $z$ ). As a means to quantify the polarization, we have computed ratios

$$\Pi = \left( -\text{Re} \iint E_y^* H_x \, dx \, dy \right) / \left( \text{Re} \iint (E_x^* H_y - E_y^* H_x) \, dx \, dy \right) \quad (9)$$

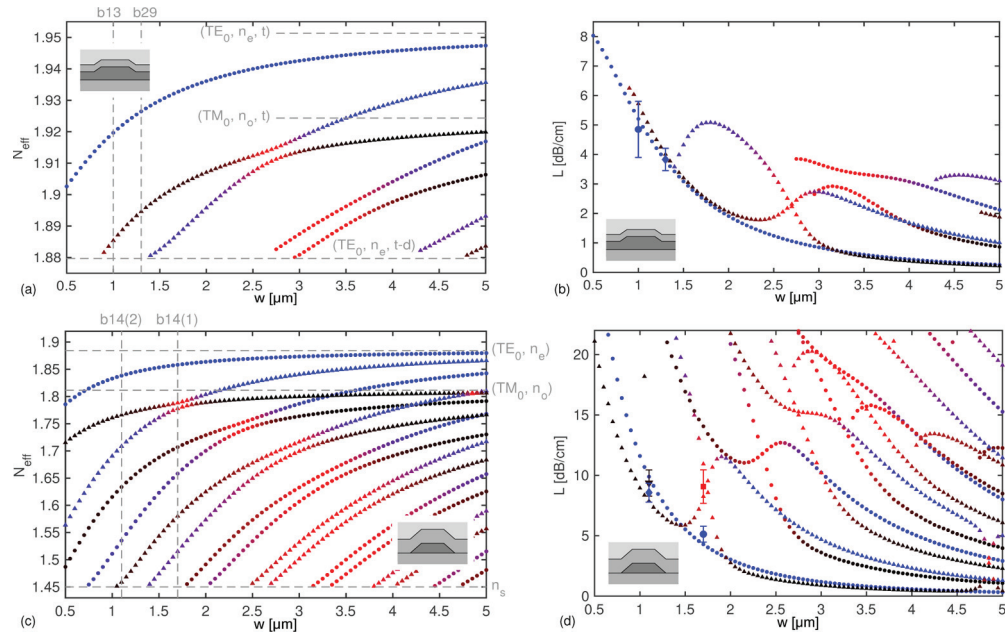


**Fig. 6.** Simulations of lossy LNOI waveguides according to Fig. 1 and Table 1, effective indices  $N_{\text{eff}}$  (a, c) and modal loss  $L$  (b, d) of guided modes as a function of waveguide top width  $w$ . Marker color indicates the polarization character  $\Pi$  (Eq. (9)), blue: TE-like, black: TM-like, red: intermediate); SYM/ASY modal parity (cf. Table 1) is distinguished by circle/triangle symbols that make up the marker lines. (a, b): Rib waveguides with the parameters of Table 1(a), columns LNOI600b13, b29. Bold markers show the measured loss data, incl. error, for the samples LNOI600b13 (circle) and LNOI600b29 (diamond). (c, d): Strip waveguides with the parameters of Table 1(a), columns LNOI450b14. Bold markers concern the measurements LNOI450b14(1) TE (circle), LNOI450b14(1) TM (square), LNOI450b14(2) TE (diamond), and LNOI450b14(2) TM (triangle).

for each mode with vectorial electromagnetic profile  $\mathbf{E}, \mathbf{H}$ . A “pure TE” field ( $E_x = 0$ ) would be characterized by  $\Pi = 1$ , while a “pure TM” field ( $H_x = 0$ ) is assigned a value  $\Pi = 0$ . Note that  $\Pi$  is not strictly limited to the range  $[0, 1]$ . Respective data has been color-coded into Fig. 6. While most configurations support modes that are of dominant TE- or TM- polarization, in Figs. 6(a) and 6(c) one observes pronouncedly hybrid, not clearly TE- or TM-polarized modes near the avoided crossings, where curves associated with modes of equal parity repel each other.

Concerning the loss, Figs. 6(b) and 6(d) show the following trends. For each individual mode one observes a decrease of loss with growing  $w$ , due to a reduction of the relative field strength of the widening profile at the channel sidewalls. Unfortunately, in general there are no optimum widths with lowest loss. For a waveguide with a specific width  $w$ , one of the modes with the strongest confinement, i.e. one of the two lowest order modes, show the lowest losses; for the present structures this is mostly the TM-like mode. Exceptions from these general trends can be seen at the very onset of some of the modal curves. Examples are local loss maxima seen for the first order TE-like mode beyond  $w = 1.4 \mu\text{m}$  in Fig. 6(a, b), or the sequence for the hybrid modes for  $w$  beyond  $2.7 \mu\text{m}$ ,  $3.8 \mu\text{m}$ ,  $4 \mu\text{m}$  in Fig. 6(c, d). Here the mode field changes, with growing  $w$ , from a wide-spread wave with correspondingly lower relative field strength at the sidewall, to a properly confined profile. Another exception are the regions with strong modal hybridization, such as around the TM measurement for sample LNOI450b14(1) in Fig. 6(c, d). Along with the

effective indices, also the loss curves change between polarization-related branches, leading to intermediate loss levels.

This last feature is seen also for the TM measurements for sample LNOI450b14(1). The waveguide supports lowest order modes  $TM_{00}$  and  $TE_{01}$  of parity class ASY with close effective indices. Both modes are pronouncedly hybrid, with polarization ratios  $\Pi = 0.39$  ( $TM_{00}$ , cf. Table 1(b)) and  $\Pi = 0.61$  ( $TE_{01}$ ). Figure 7 shows the electric parts of the related mode profiles. This explains the slightly irregular appearance, when compared to the other modes, of the TM profile of sample LNOI450b14(1) in Fig. 4(e). Also the rather different TE and TM losses measured for sample LNOI450b14(1), in light of much closer levels for sample LNOI450b14(2), can be understood in this way.

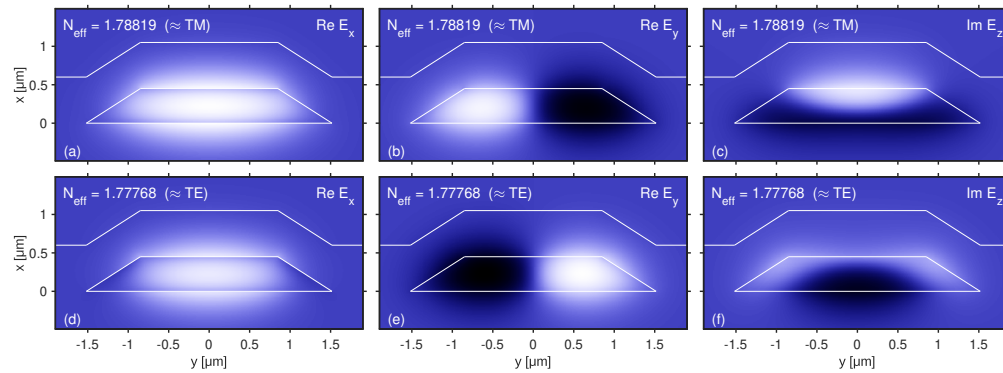


**Fig. 7.** Vectorial profiles of the two lowest order modes with symmetry class ASY of sample LNOI450b14(1); the Cartesian components  $E_x$ ,  $E_y$ , and  $E_z$  of the electric field are shown. The phase of the profiles has been adjusted such that  $E_x$  and  $E_y$  become real, while  $E_z$  is imaginary. Color levels are comparable between panels in each row.

Assuming that the facet of sample LNOI450b14(1) is illuminated by a focused, left-right symmetric TM ( $x$ -) polarized wave, both modes of Fig. 7 will be excited with amplitudes of similar magnitude, with a phase such that their  $E_x$  components add, while the  $E_y$  components interfere destructively. When these modes propagate along the channel with slightly different propagation constants, their relative phase changes. At some distance, the phase is such that components  $E_x$  cancel partly, while there is constructive interference for  $E_y$ . One thus expects an interference pattern that leads to substantial polarization conversion, with a characteristic half-beat length  $L_c = \lambda / (2 \Delta N_{\text{eff}}) \approx 74 \mu\text{m}$ . Here  $\Delta N_{\text{eff}}$  is the difference between the two effective indices. Thus, the experiment LNOI450b14(1) TM probably involved both modes, for which our estimations predict close loss levels. Perhaps these mechanisms could explain the rather large uncertainty of the measurement.

## 7. Concluding remarks

Based on a few measurements of propagation loss for practically relevant TFLN / LNOI channel waveguides, and assuming that the loss can be attributed to roughness induced scattering from the waveguide sidewalls, we have established a simple perturbational model that predicts loss levels for waveguides with different shapes. The technique requires the rigorous numerical mode analysis of the channels with their anisotropic cores. Specifically, we have looked at the width dependence of effective indices and attenuation constants of hybrid guided modes supported by potentially multimode TFLN rib and strip waveguides in an X-cut, Y-propagation configuration. Regimes with nearly degenerate, pronouncedly hybrid modes can be identified, where alongside the anti-crossing of effective indices also the attenuation curves cross, leading to otherwise

unexpected higher levels. We expect that the simple estimation procedure can aid the design of TFLN-based integrated photonic circuits in all areas where optical losses are of relevance.

Among the configurations considered, low attenuation can be expected for channels with small relative modal field strengths at the sidewalls, i.e. for the fundamental modes in wide, slab-like waveguides. This applies to channels of both rib (Fig. 6(a, b)) and strip form (Fig. 6(c, d)), where, as a trend, the levels for the less-confining rib waveguides are a little lower. Unfortunately this then leads to highly multimode channels that are not compatible with many device concepts. Hence, in general, the design objective “low loss” cannot be used on its own, say for the selection of a basic waveguide cross section, but will have to be traded off versus other targets in a design process for the entire integrated circuit.

While our model captures adequately the decline of optical power carried by particular guided modes, it does not distinguish between conversion of power to other co-propagating guided modes, of the same or different polarization, where possible (symmetry constraints), to counter-propagating guided modes, or to non-guided, radiated fields of whatever direction and polarization (the actual radiation losses). According to standard expressions from coupled mode theory [32,47], and in line with respective loss models [28,29], all these effects should in principle be driven by the squared local optical electric field at the sidewalls (attributed to *both* modes involved, where applicable, though), and as such be covered roughly by our perturbational expressions.

On the one hand, further measurements, for samples prepared in a uniform way, would be desirable to strengthen the experimental basis. Then perhaps extended loss models could become meaningful that take a dependence on sidewall orientation, local field polarization, or external layering into account. Within the present formalism, this “anisotropy” could be implemented through a non-scalar, diagonal (polarization) or non-diagonal (sidewall angle) perturbational loss tensor in place of the present scalar expression (4).

On the other hand, in principle just one measurement suffices to fit the single free parameter  $\epsilon''$  involved in the simpler isotropic model. With that, one could predict curves like the ones in Figs. 6(b, d), with an uncertainty as given by the differences of the values in row  $\epsilon''$  of Table 1. According to Eq. (5), however, the dependence on waveguide geometry on the attenuation coefficients  $\alpha$  is given entirely by the purely numerically determined modal overlaps  $Q$ . Hence, by accepting the underlying perturbational model one could even theoretically assess the trends in the influence of the waveguide shape on the propagation loss for an unknown waveguide configuration, *without* any measurements at all.

**Funding.** Deutsche Forschungsgemeinschaft (231447078–TRR 142/3-2022 (B06, C11)); Ministry of Culture and Science of the state of North Rhine-Westphalia (PhoQC); Max Planck School of Photonics.

**Acknowledgment.** Silia Babel is part of the Max Planck School of Photonics supported by the German Federal Ministry of Education and Research (BMBF), the Max Planck Society, and the Fraunhofer Society.

**Disclosures.** The authors declare no conflicts of interest.

**Data availability.** Data underlying the results presented in this paper are not publicly available at this time but may be obtained from the authors upon reasonable request.

## References

1. R. S. Weis and T. K. Gaylord, “Lithium niobate: summary of physical properties and crystal structure,” *Appl. Phys. A* **37**(4), 191–203 (1985).
2. J. Lu, J. B. Surya, X. Liu, *et al.*, “Periodically poled thin-film lithium niobate microring resonators with a second-harmonic generation efficiency of 250,000%/W,” *Optica* **6**(12), 1455–1460 (2019).
3. C. J. Xin, J. Mishra, C. Chen, *et al.*, “Spectrally separable photon-pair generation in dispersion engineered thin-film lithium niobate,” *Opt. Lett.* **47**(11), 2830–2833 (2022).
4. C. Wang, C. Langrock, A. Marandi, *et al.*, “Ultrahigh-efficiency wavelength conversion in nanophotonic periodically poled lithium niobate waveguides,” *Optica* **5**(11), 1438–1441 (2018).
5. Z. Ma, J.-Y. Chen, M. Garikapati, *et al.*, “Highly efficient and pure few-photon source on chip,” *Phys. Rev. Appl.* **20**(4), 044033 (2023).

6. L. Ledezma, R. Sekine, Q. Guo, *et al.*, “Intense optical parametric amplification in dispersion-engineered nanophotonic lithium niobate waveguides,” *Optica* **9**(3), 303–308 (2022).
7. C. Wang, M. Zhang, X. Chen, *et al.*, “Integrated lithium niobate electro-optic modulators operating at CMOS-compatible voltages,” *Nature* **562**(7725), 101–104 (2018).
8. D. Pohl, A. Messner, F. Kaufmann, *et al.*, “100-GBd waveguide Bragg grating modulator in thin-film lithium niobate,” *IEEE Photonics Technol. Lett.* **33**(2), 85–88 (2021).
9. D. Renaud, D. R. Assumpcao, G. Joe, *et al.*, “Sub-1 Volt and high-bandwidth visible to near-infrared electro-optic modulators,” *Nat. Commun.* **14**(1), 1496 (2023).
10. F. Yang, X. Fang, X. Chen, *et al.*, “Monolithic thin film lithium niobate electro-optic modulator with over 110GHz bandwidth,” *Chin. Opt. Lett.* **20**(2), 022502 (2022).
11. M. Yu, D. I. Barton, R. Cheng, *et al.*, “Integrated femtosecond pulse generator on thin-film lithium niobate,” *Nature* **612**(7939), 252–258 (2022).
12. D. Jia, R. Zhang, C. Yang, *et al.*, “Electrically tuned coupling of lithium niobate microresonators,” *Opt. Lett.* **48**(10), 2744–2747 (2023).
13. A. Shams-Ansari, G. Huang, L. He, *et al.*, “Reduced material loss in thin-film lithium niobate waveguides,” *APL Photonics* **7**(8), 081301 (2022).
14. C. Wei, J. Li, Q. Jia, *et al.*, “Ultrahigh-Q lithium niobate microring resonator with multimode waveguide,” *Opt. Lett.* **48**(9), 2465–2467 (2023).
15. C. Li, J. Guan, J. Lin, *et al.*, “Ultra-high Q lithium niobate microring monolithically fabricated by photolithography assisted chemo-mechanical etching,” *Opt. Express* **31**(19), 31556–31562 (2023).
16. D. F. Walls and G. J. Milburn, *Quantum optics* (Springer-Verlag, Berlin, Heidelberg, 2008).
17. D. Bonneau, G. J. Mendoza, J. L. O’Brien, *et al.*, “Effect of loss on multiplexed single-photon sources,” *New J. Phys.* **17**(4), 043057 (2015).
18. J. L. O’Brien, “Optical quantum computing,” *Science* **318**(5856), 1567–1570 (2007).
19. D. Melati, A. Melloni, F. Morichetti, *et al.*, “Real photonic waveguides: guiding light through imperfections,” *Adv. Opt. Photonics* **6**(2), 156–224 (2014).
20. F. P. Payne and J. P. R. Lacey, “A theoretical analysis of scattering loss from planar optical waveguides,” *Opt. Quantum Electron.* **26**(10), 977–986 (1994).
21. J. P. R. Lacey and F. P. Payne, “Radiation loss from planar waveguides with random wall imperfections,” *IEE Proc. J Optoelectron. UK* **137**(4), 282–289 (1990).
22. D. Melati, F. Morichetti, A. Melloni, *et al.*, “A unified approach for radiative losses and backscattering in optical waveguides,” *J. Opt.* **16**(5), 055502 (2014).
23. K. K. Lee, D. R. Lim, H.-C. Luan, *et al.*, “Effect of size and roughness on light transmission in a Si/SiO<sub>2</sub> waveguide: Experiments and model,” *Appl. Phys. Lett.* **77**(11), 1617–1619 (2000).
24. T. Barwicz and H. A. Haus, “Three-dimensional analysis of scattering losses due to sidewall roughness in microphotonic waveguides,” *J. Lightwave Technol.* **23**(9), 2719–2732 (2005).
25. S. G. Johnson, M. L. Povinelli, M. Soljačić, *et al.*, “Roughness losses and volume-current methods in photonic-crystal waveguides,” *Appl. Phys. B* **81**(2-3), 283–293 (2005).
26. C. Ciminelli, F. Dell’Olio, V. M. N. Passaro, *et al.*, “Fully three-dimensional accurate modeling of scattering loss in optical waveguides,” *Opt. Quantum Electron.* **41**(4), 285–298 (2009).
27. S. Hörmann, J. W. Hinum-Wagner, A. Bergmann, *et al.*, “An ab initio, fully coherent, semi-analytical model of surface-roughness-induced scattering,” *Journal of Lightwave Technology* **41**, 1503–1510 (2023).
28. C. G. Poulton, C. Koos, M. Fujii, *et al.*, “Radiation modes and roughness loss in high index-contrast waveguides,” *IEEE J. Sel. Top. Quantum Electron.* **12**(6), 1306–1321 (2006).
29. I. Papakonstantinou, R. James, D. R. Selviah, *et al.*, “Radiation- and bound-mode propagation in rectangular, multimode dielectric, channel waveguides with sidewall roughness,” *J. Lightwave Technol.* **27**(18), 4151–4163 (2009).
30. K. P. Yap, A. Delâge, J. Lapointe, *et al.*, “Correlation of scattering loss, sidewall roughness and waveguide width in silicon-on-insulator (SOI) ridge waveguides,” *J. Lightwave Technol.* **27**(18), 3999–4008 (2009).
31. S. M. Lindercrantz and O. G. Hellesø, “Estimation of propagation losses for narrow strip and rib waveguides,” *IEEE Photonics Technol. Lett.* **26**(18), 1836–1839 (2014).
32. C. Vassallo, *Optical Waveguide Concepts* (Elsevier, Amsterdam, 1991).
33. L. Ebers, A. Ferreri, M. Hammer, *et al.*, “Flexible source of correlated photons based on LNOI rib waveguides,” *J. Phys. Photonics* **4**(2), 025001 (2022).
34. L. Ebers, A. Ferreri, M. Hammer, *et al.*, “Corrigendum: Flexible source of correlated photons based on LNOI rib waveguides (2022 J. Phys. Photonics 4 025001),” *J. Phys. Photonics* **5**(2), 029501 (2023).
35. M. Hammer, “PlasS — 1-D mode solver for complex optical multilayer step-index slab waveguides,” <https://www.computational-photonics.eu/plas.html>.
36. W. Karthe and R. Müller, *Integrierte Optik* (Akademische Verlagsgesellschaft Geest & Portig K.-G., Leipzig, 1991).
37. M. Lohmeyer, *Guided waves in rectangular integrated magneto-optic devices* (Cuvillier Verlag, Göttingen, 1999). Dissertation, Universität Osnabrück.
38. V. S. Ilchenko, A. A. Savchenkov, A. B. Matsko, *et al.*, “Nonlinear optics and crystalline whispering gallery mode cavities,” *Phys. Rev. Lett.* **92**(4), 043903 (2004).



39. X. R. Yu, M. K. Wang, J. H. Li, *et al.*, “Study on the single-mode condition for x-cut LNOI rib waveguides based on leakage losses,” *Opt. Express* **30**(5), 6556–6565 (2022).
40. S. Babel, L. Bollmers, M. Massaro, *et al.*, “Demonstration of Hong-Ou-Mandel interference in an LNOI directional coupler,” *Opt. Express* **31**(14), 23140–23148 (2023).
41. F. Kaufmann, G. Finco, A. Maeder, *et al.*, “Redeposition-free inductively-coupled plasma etching of lithium niobate for integrated photonics,” *Nanophotonics* **12**(8), 1601–1611 (2023).
42. R. Regener and W. Sohler, “Loss in low-finesse Ti:LiNbO<sub>3</sub> optical waveguide resonators,” *Appl. Phys. B* **36**(3), 143–147 (1985).
43. M. Santandrea, *Design of nonlinear integrated devices for quantum optics applications* (Paderborn University, Paderborn, Germany, 2019). Ph.D. Thesis.
44. JCMwave GmbH, Berlin, Germany; <https://www.jcmwave.com>.
45. W. H. Press, S. A. Teukolsky, W. T. Vetterling, *et al.*, *Numerical Recipes in C*, 2nd ed. (Cambridge University Press, 1992).
46. M. Hammer, “OMS — 1-D mode solver for dielectric multilayer slab waveguides,” <https://www.computational-photonics.eu/oms.html>.
47. D. G. Hall and B. J. Thompson, eds., *Selected Papers on Coupled-Mode Theory in Guided-Wave Optics*, vol. MS 84 of *SPIE Milestone Series* (SPIE Optical Engineering Press Bellingham, Washington USA, 1993).